Anisotropy effect of bioinspired ceramic/ceramic composites: Can the platelet orientation enhance the mechanical properties at micro- and submicrometric length scale?

N. Abando[1], H. Saad[2], M. A. Monclús[3], S. Deville[2], J. Molina-Aldareguia[3], J.J. Roa[1,4,*]

[1] Department of Mechanical Engineering (CIEFMA). Barcelona School of Engineering (EEBE). Technical University of Catalonia-BarcelonaTech, Barcelona 08019, Spain
[2] Laboratoire de Synthèse et Fonctionnalisation des Céramiques, UMR308 CNRS/Saint-Gobain CREE, Saint-Gobain Research Provence, Cavaillon, France
[3] IMDEA Materials Institute, Calle Eric Kandel 2, Getafe, 28906 Madrid, Spain
[4] Research Center in Multiscale Science and Engineering. Barcelona School of Engineering (EEBE). Technical University of Catalonia-BarcelonaTech, Barcelona 08019, Spain

* Corresponding author, e-mail: joan.josep.roa@upc.edu

Abstract: In advanced ceramics, improving toughness usually relies on the introduction of a soft metallic or polymeric ductile phase, which decreases the mechanical properties. Some natural materials are strong, stiff and tough due to a combination of mechanisms operating at different length scales. However, such structures have been extremely difficult to replicate into synthetic materials. Here we investigate the microstructure and the micromechanical properties of a bioinspired ceramic-ceramic composite. The micromechanical properties at room temperature show slight differences as a function of the platelet orientation. The hardness strongly decreases with increasing temperatures (up to 550 ºC) for all the investigated orientations. The plasticity index, defined as the H/E ratio, was used to estimate the fracture toughness of this material, measured in the 7.2 – 9.9 MPa·√m range.

Keywords: Bioinspired materials; ceramic/ceramic composites; mechanical anisotropy; nanoindentation; fracture mechanisms.

1. Introduction

In general, improving fracture toughness of a material decreases its hardness. In ceramic materials, improved fracture toughness can be achieved by the addition

of a soft ductile phase, which thus reduces the inherent brittleness of such materials. To improve the hardness and stiffness required for its final structural application, a large amount of inorganic and/or organic elements can be incorporated, even surpassing the 95% vol. [1,2].

Many natural materials are both strong and tough. The literature on bio-inspired materials is extensive in number of published papers dealing with multiple biological systems, including: woodpecker [1], nacre [2,3], desert scorpion [4], arterial walls [5], elk antlers [6,7,8,9], porcupine quills [10], horse hooves [11,12], sea snail eggs [13,14], buriti palm [15], pomelo fruit [16], plant tissues [17], flax [18], kelp [19], among others. It is also broad in terms of the methodology employed to characterize these complex materials (i.e. mechanical characterization, numerical modeling, environmental assessment, composite fabrication and prototyping, among others) as well as the length scale at which the properties were evaluated. Bioinspired designs are thus promising to enhance the fracture toughness of engineering and structural materials.

A commonly reported strategy to enhance the fracture toughness is to alternate layers of weak and ductile materials between brittle inorganic layers which delay crack propagation [2,3]. Nacre is a well-known example of such microstructure, with hard microscale mineral layers bonded together by soft organic layers. Accordingly, whenever a crack nucleates, it quickly encounters an organic layer, which provides avenues for crack deflection and energy dissipation. Cracks in such microstructures can thus be controlled and stopped before spreading through the whole shell, causing serious damage. However, ductile layers in such synthetic designs are either polymeric or metallic; and hence, the composite materials cannot thus be used at high temperature.

Bioinspired brick-and-mortar ceramic/ceramic designs have recently proven able to combine high strength and high toughness up to reasonably high temperatures (600°C) [20,21,22,23]. They are made of anisotropic alumina platelets, bonded by a glassy interphase with various compositions.

Despite the importance of the mechanical behavior of such structures at the micro-scale, there are very scarce studies of their micromechanical properties, which have mainly focused on macro-scale properties [24,25]. The role of the lamella orientation, for instance, is still unclear. A deeper knowledge of the deformation behavior of such materials as a function of lamellar orientation and

temperature at the micro-scale is crucial in order to improve the performance of these materials and to enhance their lifetime under severe working conditions.
Here, we conducted a systematic micro- and nanomechanical study of strong, tough and stiff bio-inspired ceramic samples made from brittle constituents. In order to correlate the mechanical properties at different length scales with the microstructure, we investigated three different platelet orientations. Special attention was paid to analyze the main damage and fracture mechanisms as a function of the platelet orientation by FESEM/FIB.

2. Material and methods

2.1. Material

The ceramic/ceramic composite specimens were processed combining a freeze-drying technique together with Field-Assisted Sintering Technology (FAST). Once the suspension with the Al2O3 platelets is frozen with liquid nitrogen, it is freeze-dired in order to avoid platelet agglomeration. The sintering, on the other side, allows the user to keep a fine microstructure of the material due to the short heating time. More information about the processing route is available in Refs. [26,27,28]. Three microstructurally different ceramic/ceramic composites or alumina/glassy phase composite materials with different platelet orientation were investigated. The glassy phase presents the following chemical composition (in wt.%); 10 % SiO_2 + 65 % CaO + 25 % Al_2O_3. Samples were designated as "S_i", where the subscript *i* denotes the platelet orientation from the indentation plane. We investigated three different orientations: S_0, S_{45} and S_{90}.
A scanning electron microscopy (SEM) image for the ceramic/ceramic composite with a 45º platelet orientation (sample S_{45}) is shown in **Figure 1**.

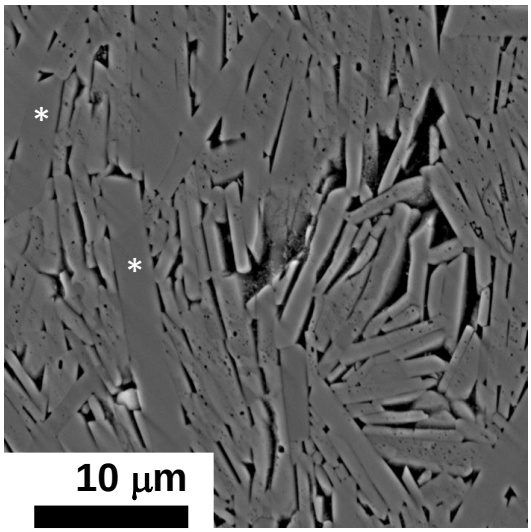

Figure 1. SEM micrograph of the S_{45} composite. A few large platelets are observed labelled with * and the black areas corresponds to porosity heterogeneously distributed in the observed region.

After the field assisted sintering process, the specimens' density was measured with the Archimedes' principle, using distilled water as the buoyant medium.

Prior to the chemical, microstructural, and mechanical characterization, each surface to be tested was polished on an ordinary metallographic polisher with diamond paste down to 3 μm grade size, with a final polishing step with colloidal silica. The quality of the finishing was checked by confocal laser scanning microscopy (CLSM) in order to avoid the presence of scratches on the surfaces. Finally, all specimens were cleaned by means of ultrasounds with acetone for 10 min and dried with pure air.

2.2. Microstructural characterization

The chemical composition analysis through the sample thickness was carried out using a dual beam Workstation (Zeiss Neon 40) equipped with an energy-dispersive X-ray detector (EDX). This device allows the detection of all elements between boron and uranium and the quantification of elements with $11 \leq Z \leq 92$. EDX was used to perform a linear chemical profile through the alumina platelets to detect changes in the composition of Al, Si, Ca and Na components. The measurements were performed with an acceleration voltage of 15 kV and at a constant working distance of 35 mm.

2.3. Mechanical properties: hardness and elastic modulus

The mechanical response at the micro- and submicrometric length scale was evaluated as a function of the platelet orientation as depicted in **Figure 2**. The evaluation of hardness (*H*) and elastic modulus (*E)* was made at room temperature (RT) as well as at different increasing temperatures (up to 550 ºC) by using the nanoindentation technique.

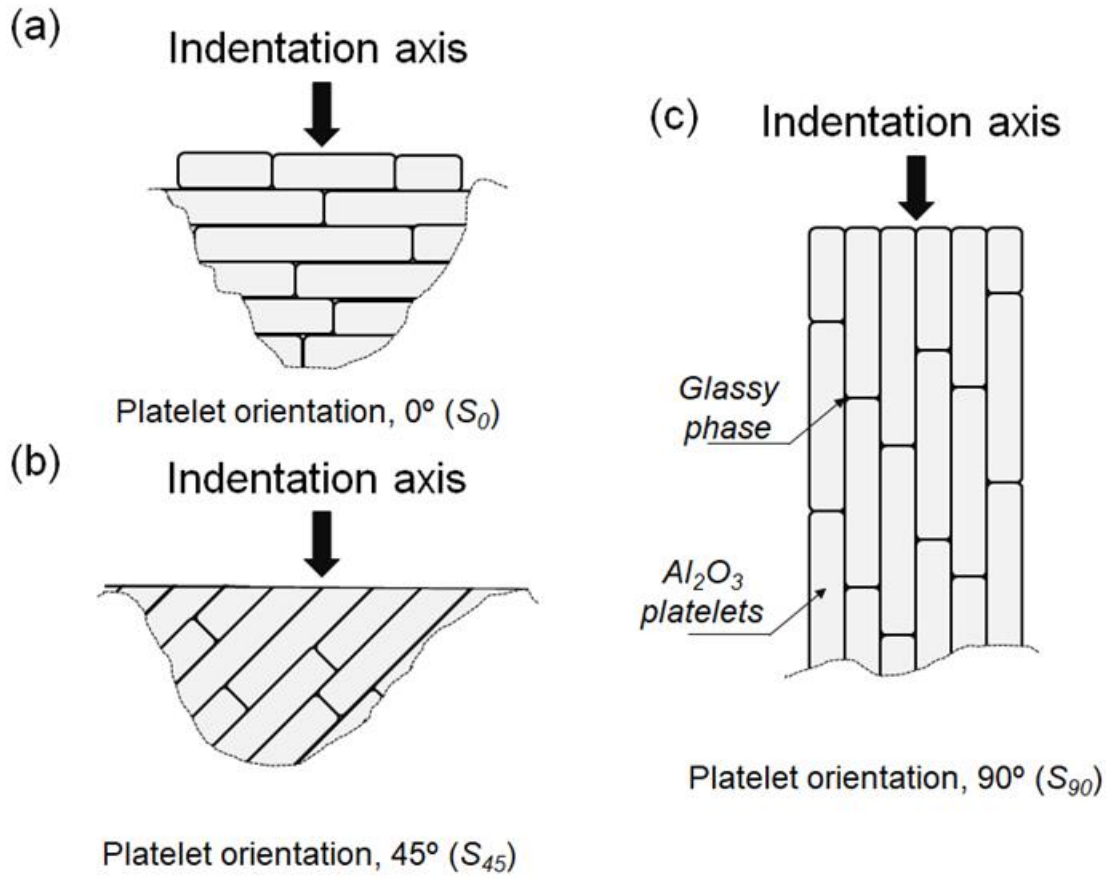

Figure 2. Schematic representation of the indentation axis as a function of the different platelet orientations for the different specimens investigated here: a) S_0, b) S_{45} and c) S_{90} with respect to the indentation axis.

Nanoindentation tests at RT were performed on a Nanoindenter XP (MTS) with a Berkovich diamond tip. This equipment worked with the continuous stiffness measurement mode (CSM) technique, allowing a dynamic determination of the mechanical properties during the indentation process. A homogeneous array of 16 imprints (4 by 4) was conducted at 2000 nm of maximum displacement into the surface or until reaching the maximum applied load of the loading cell (650 mN). The distance between imprints was kept at 50 μm in order to avoid any overlapping effect between them. Such conditions guaranteed that each individual test could be treated as an independent statistical event. Moreover, the loading/unloading as well as the peak holding times were kept constant for all

imprints. The strain rate was held constant at 0.05 s^{-1} and the tip indenter was carefully calibrated by indenting a fused silica standard of well-known Young's modulus, 72 GPa.

Moreover, different nanoindentation tests at RT and at high temperature were conducted using the TI 950 Triboindenter (Hysitron). For high temperature nanoindentation testing, a hot stage (Hysitron xSol) and a Berkovich diamond indenter fitted to a special long insulating shaft were used. In this configuration, the sample is placed between two resistive heating elements in order to eliminate temperature gradients across the sample thickness. Dry air and argon around the tip and sample surface were used to purge the testing area to prevent heated gases reaching the transducer and reduce possible oxidation. Once the sample reached the selected temperature (25, 100, 200, 300, 400, 500 and 550 ºC) and was stable at the target temperature to within ± 0.1 ºC, the tip was placed at 100 μm from the sample surface for 10-15 minutes, to ensure passive heating of the tip before the start of the test and minimize thermal drift.

At least eight indents per temperature were performed at different positions under load control, using loading and unloading rates of 3.5 $mN \cdot s^{-1}$, with a maximum applied load of 13 mN and a holding time of 20 s. Reduced elastic modulus (E_r) and hardness were determined form the recorded load-displacement curves using the Oliver and Pharr equations [29,30].

Five imprints per load and specimen were done at micrometric length scale in order to determine the average Vickers hardness of the ceramic/ceramic composite. Six different applied loads (0.5, 1, 5, 10, 30 and 50 kgf) were tested. In addition to obtaining the Vickers hardness (HV), this method was also used for measuring the resistance to cracking by sharp contact. The holding time was kept constant at 10 s.

2.4. Microstructural characterization and damage by contact loading evaluation

Microstructural and surface damage analyses of all the specimens were performed by scanning electron microscopy (SEM) using a Phenom XL Desktop SEM (Thermofisher) at an acceleration voltage of 5 kV.

Microstructural changes and fracture mechanisms induced during the indentation process were characterized by micro-machining cross-sections below the

indented surface by means of focused ion beam (FIB). Cross-sectioning and field emission scanning electron microscopy (FESEM) observations were conducted using a dual beam Workstation (Zeiss Neon 40). A thin platinum layer was deposited on the region of interest prior to FIB with the main aim of reducing ion-beam damage. Then, a Ga^+ ion source was used to mill the surface at a voltage of 30 kV. A final polishing of the cross-section was performed at a current of 500 pA in order to get more details related to microstructural effects and the damage induced.

3. Results and discussion

3.1. Microstructural characterization

After the sintering process, the ceramic/ceramic composites presented a heterogeneous microstructure composed of alumina (Al_2O_3) platelets and a minor secondary phase mainly based on silicon oxide (SiO_2) and calcium carbonate ($CaCO_3$), located between the platelets. **Figure 3** shows the SEM micrographs of the ceramic/ceramic composites with 0 and 90º oriented platelets. The 45º oriented sample (not shown here) has a microstructure similar to the 90º sample. The spatial distribution of the main elements of the glassy phase (SiO_2 + $CaCO_3$) inside the heterogeneous microstructure was characterized by EDX performed on a FIB cross-section extracted from the selected area for S_{45} (**Figure 4a**).

The EDX spectra (see **Figure 4b**) shows the spatial distribution of Al, Si, Ca and Na through several interfaces between the Al_2O_3 platelets of the sample of study. The Ca and Na profiles present a homogeneous distribution along the different interfaces. However, along the analyzed profiles, three different regions with a lower amount of Al and higher amount of Si (labelled by * in **Figure 4b**) were detected. This observation confirms that the glassy phase, mainly constituted by SiO_2, is located at the interface between the Al_2O_3 platelets. A similar chemical distribution was observed for the other two specimens (S_0 and S_{90}), not shown here.

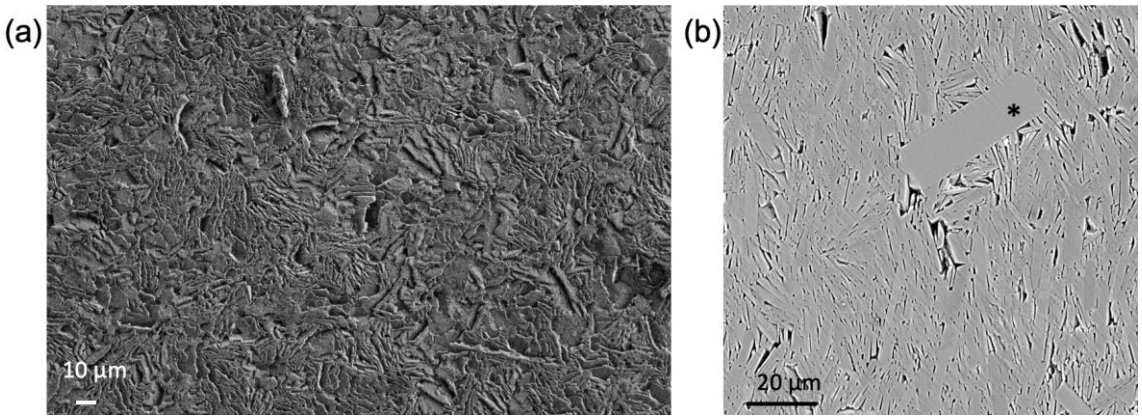

Figure 3. SEM micrograph of the ceramic/ceramic composite with different platelet orientation: (a) S_0 and (b) S_{90}.

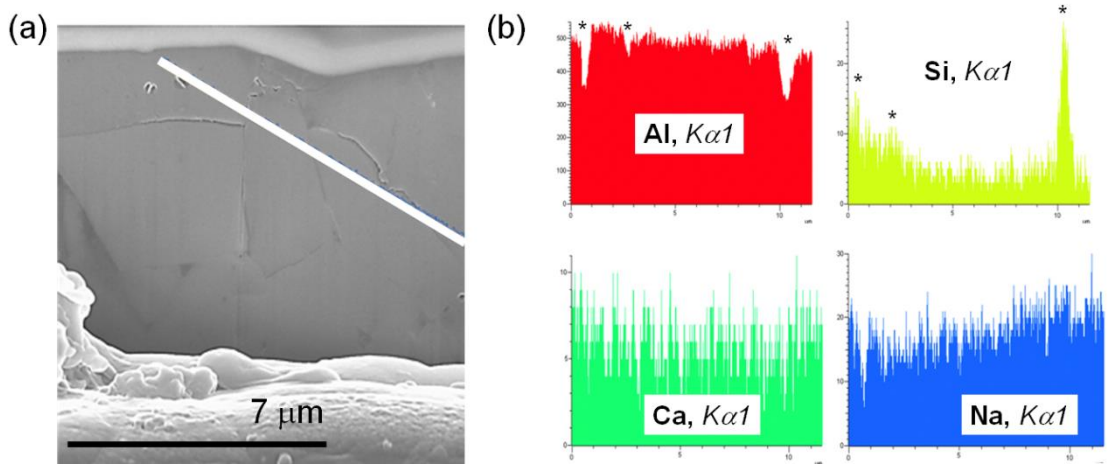

Figure 4. (a) FIB cross-section micrograph and (b) EDX profile along the entire white line in **Figure 4a** for Al (red), Si (yellow), Ca (green) and Na (blue).

3.2. Mechanical properties

Vickers hardness values as a function of the applied load are is shown in **Figure 5** for samples S_{45} and S_{90}. No results could be obtained for the S_0 specimen due to the chipping effect caused by the indentation process, where a crack can sometimes be generated, which propagates along the basal plane until it reaches the surface, inducing chipping of the material. As a consequence of the loss of material, there are no imprints to be measured as shown in **Figure 6**. Moreover, for applied loads greater than 5 kgf, the Vickers hardness could not be evaluated for the S_{45} specimen because the activated fracture mechanisms did not allow to correctly measure the diagonals of the residual imprint, as detailed in **section 3.4**. The Vickers hardness measured at 5 kgf in the S_{45} specimen (**Figure 5**) is slightly lower than that obtained for the S_{90}. This reduction in hardness is related to the final 3D-microstructure and the higher pore density for S_{45} with respect to

S_{90} sample, as visible in both FIB-cross sections for the S_{45} presented in **Figure 11**.

Two different regions were observed in the plot of hardness (*H*) versus applied load (*P*) presented in **Figure 5**. In the first region, which corresponds to low applied loads (*P ≤ 5 kgf*), the hardness increases, which may be associated to three different phenomena: i) indentation size effect (ISE) [31], ii) a scale effect phenomenon (i.e. surface topography due to the different in hardness between each constitutive phase and possible indenter tip defects), and iii) confinement of plastic deformation field inside of an Al_2O_3 platelet at low applied loads, so that hardness values presented in **Figure 5** corresponds to the intrinsic hardness of the hardest component and not of the composite material. In the second region, corresponding to high applied loads (*P > 5 kgf*), hardness values fall within a stable regime for S_{90}. Vickers hardness obtained at 5 kgf are summarized in **Table 1**.

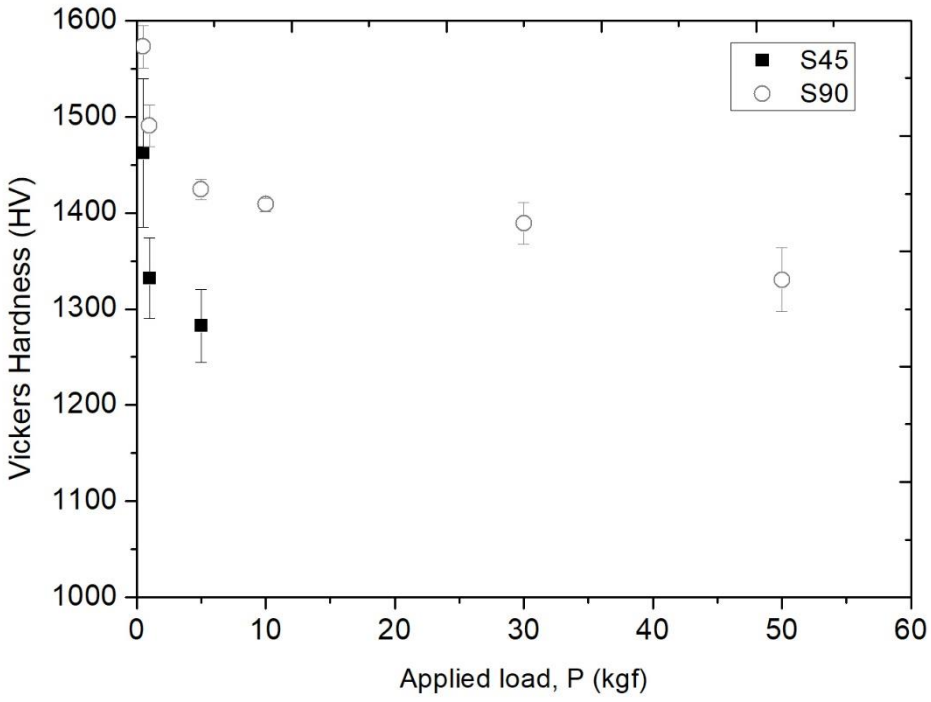

Figure 5. Vickers hardness trend for each specimen as a function of the applied load.

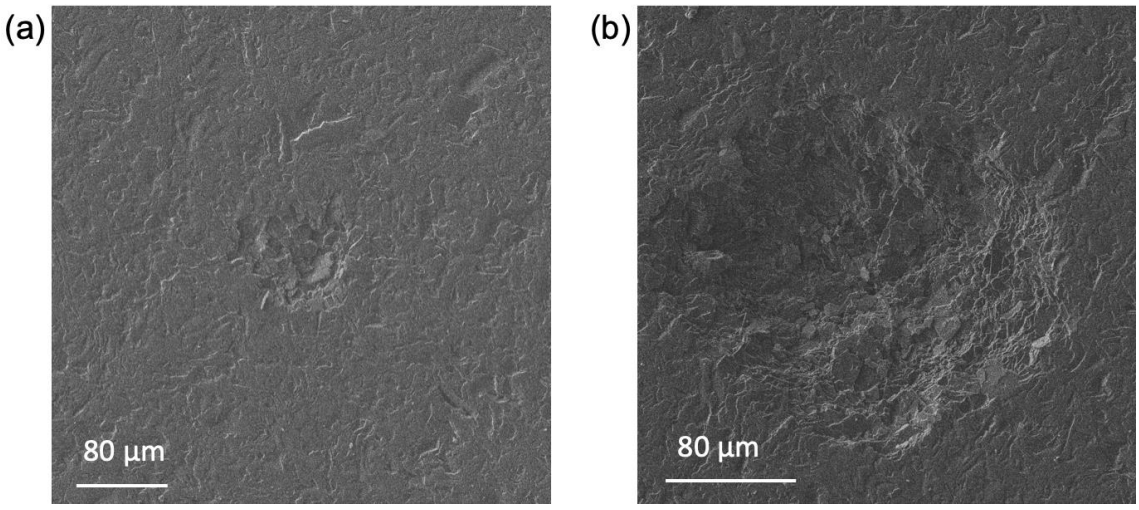

Figure 6. Chipping effect observed in the 0º oriented sample at a) 1 kgf and b) 10 kgf applied load.

The S_0 specimen exhibited a strong heterogeneity in terms of micromechanical properties, as observed in the plots of hardness as a function of the displacement into the surface acquired with CSM, for which two representative plots are depicted in **Figure 7**. All the curves present a drop of hardness for displacement into surface higher than 700 nm, which may be associated with the internal porosity present inside the material as depicted in **Figure 4a**.

This heterogeneity in the composite's mechanical response is associated with its chaotic microstructure (see **Figure 3a**). Because of the lack of consistent behavior, the S_0 oriented sample was excluded in some of the comparison studies with the other S_{45} and S_{90} oriented samples.

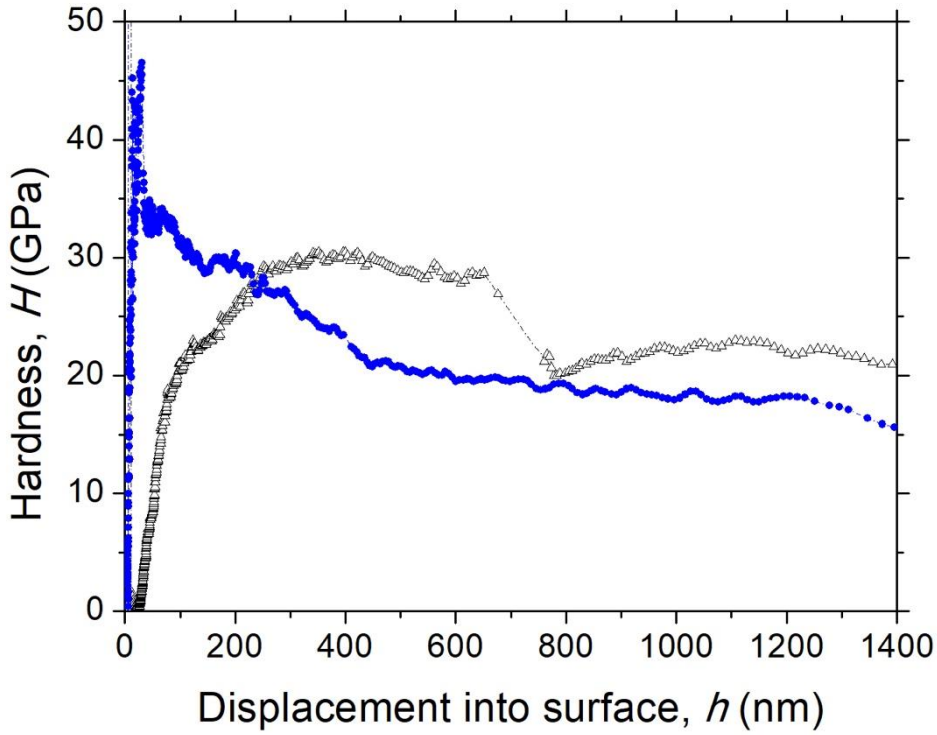

Figure 7. Hardness vs. displacement into surface (*H vs. h*) curves that belong to two different nanoindentations made in the S_0 sample.

The RT hardness and the elastic modulus as a function of the displacement into the surface for the S_{45} and S_{90} samples are plotted in **Figures 8a** and **8b** respectively and summarized in **Table 1**. The variation and scatter associated with the hardness measurement at low indentation depths ($h \leq 500$ nm) may be directly related to a scale effect phenomenon (i.e. surface topography and possible indenter tip defects). On the other hand, for penetration depths higher than 500 nm, the micromechanical properties for both composites were found to approach constant values, independent of the Al_2O_3-platelet orientation. It can be appreciated that the specimen with a platelet orientation perpendicular to the indentation axis presents a hardness value close to 24 GPa, while the Al_2O_3-platelets oriented at 45º present a hardness reduction of around 8%.

As observed in **Figure 8b**, and reported in **Table 1,** the elastic modulus remains constant at ~ 400 GPa for the S_{45} and S_{90}. For penetration depths higher than 250 nm, for which the elastic field spans at least 5 μm (~ 20 times the displacement into surface), several Al_2O_3-platelets and glassy phase interfaces are probed by the indentation process, yielding as a result the elastic modulus for

the ceramic/ceramic composite. Besides, the specimen with the Al_2O_3-platelets parallel to the indentation plane is slightly stiffer (~ 7%) than the other two orientations investigated here. This phenomenon may be associated with the existence of mechanical anisotropy in terms of elastic modulus and further studies will be required to verify this hypothesis. This confirms that the ISE is not an artifact due to the indenter shape calibration. Similar study has been already carried out at the macroscopic length scale by Bouville *et al.* [23] on alumina-glass phase composite fabricated by using the ice templating methodology and reporting a flexural modulus of 290 GPa. This value is around 38% lower than those reported in **Table 1** when the Al_2O_3 platelets are oriented at 45 and 90º from the indentation axis (see **Figure 2**) and the main difference behind this difference may be associated to: (1) anisotropic effect due to the Al_2O_3 platelets are randomly oriented and (2) flexural strength tests takes into consideration the different heterogeneities created during the processing route (i.e. porosity, etc.) while the nanoindentation data provide the elastic modulus locally, where the amount of defects available in the indentation zone are reduced yielding a higher elastic modulus. Recently, Le Ferrand *et al.* [32] and Pratyush Behera [33] reported a similar trend in terms of hardness and elastic modulus as the values reported here for Al_2O_3 platelets oriented at 0 and 90º.

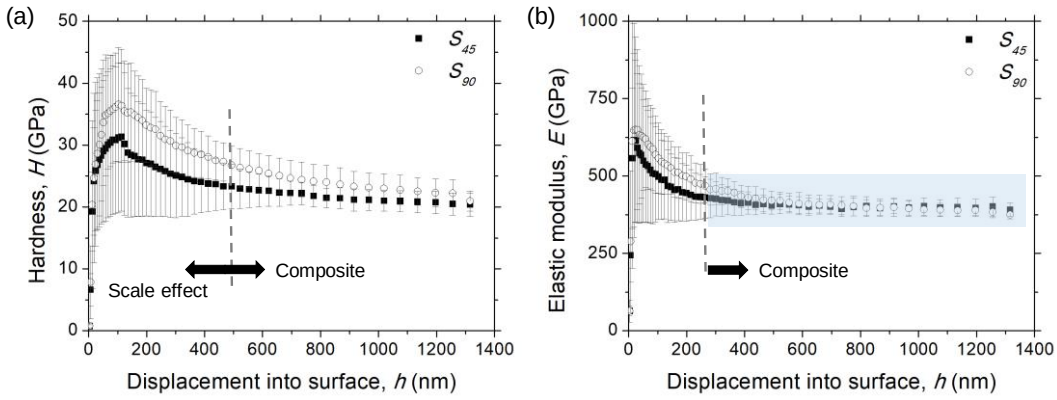

Figure 8. Micromechanical properties evolution as a function of the displacement into the surface for S_{45} and S_{90} ceramic/ceramic composites. (a) Hardness, and (b) Elastic modulus.

Table 1. Vickers hardness, hardness and elastic modulus for the three specimens investigated, assessed in the stable region (displacement into surface higher than 500 and 250 nm for the hardness and the elastic modulus, respectively).

Nomenclature	Vickers hardness, HV5	Hardness, H (GPa)	Elastic modulus, *E* (GPa)
S_0	-	23.2 ± 1.3	426 ± 4
S_{45}	1307 ± 63	21.6 ± 0.8	400 ± 5

S_{90}	1424 ± 10	24.0 ± 1.4	400 ± 11

As it is clear evident, the elastic modulus determined with the two nanoindentation set-ups at RT is different being the one determined under displacement control mode up to 2000 nm of maximum displacement into surface higher than those determined under loading control mode up to 13 mN of maximum applied load, which should be constant and independent of the applied load and the stress applied due to this is an intrinsic property of the material. This different may be associated to several factors: (1) the shallower imprints conducted at 13 mN can be affected by length scale effects (i.e. porosity near the surface as shown in **Figure 1**) and (2) also it may be attributed that one has been determined dynamically (by using the CSM modulus) yielding a higher elastic modulus compared with the one determined statically, similar trend has been reported on natural materials as reported in Ref. [34] when the material is tested under compression. A possible cause which explain this phenomenon could be the different strain rates involved in the nanoindentation tests. However, more studies in order to elucidate the strain effect is necessary to conduct. Furthermore, from the obtained results determined at different testing temperatures, it can be said that the specific microstructure of the studied composite materials leads to superior mechanical properties. In order to assess their use in harsh environments, with temperatures ranging from 300 ºC up to 550 ºC, the micromechanical properties were measured as a function of temperature (see **Figure 9**). The hardness (**Figure 9a**) is temperature-dependent for both orientations (45° and 90°) while the elastic modulus (**Figure 9b**) does not change along the investigated temperature range. The hardness value when the Al_2O_3-platelet orientation is parallel and perpendicular to the indentation axis, S_0 and S_{90} respectively, remains practically stable up to an indentation temperature of around 300 ºC. A decrease from 26 ± 2 GPa at room temperature to 16 ± 3 GPa at 550 ºC can be observed for sample S_{90}.

On the other hand, the hardness reduction for the S_{45} follows a different trend with temperature of that presented for the S_{90}. For that matter, the hardness starts to decrease for temperatures above 100 ºC (22% decrease) and remains almost constant at ~14 GPa until 500 ºC. At 550 ºC, the hardness decreases slightly possibly due to a softening of the glassy phase.

The elastic modulus of the S_{45} and S_{90} ceramic/ceramic composite (**Figure 9b**) samples remains approximately constant with increasing temperatures with values very much dependent on the orientation of the Al_2O_3-platelets with respect to the indentation axis. Sample S_{45}, with Al_2O_3-platelets oriented at 45º, present low modulus values ranging from 120 to 140 GPa. In contrast, samples with Al_2O_3-platelets oriented near the basal plane (S_0, not shown here due to the strong heterogeneity presented in **Figure 7**) and edge oriented (S_{90}) are stiffer, presenting elastic modulus values around 275 and 325 GPa. This behavior may be associated with microstructural defects like porosity. The S_{45} sample has a microstructure with an easier path and more sensitive to the strain-hardening on the apparent stiffness, resulting in an elastic modulus which is almost 50% lower than for S_0 and S_{90}. The large scatter associated with the elastic modulus gives evidence of the strong anisotropic character of the elastic properties. Furthermore, the consistency of the results in **Figure 9b**, emphasizes the high thermal stability of the experiment performed on this ceramic composite since the range of elastic modulus values is similar for each tested temperature. Furthermore, the elastic modulus for the S_{90} specimen is in fair agreement with the flexural strength modulus in Ref. [23] at the macroscopic length scale.

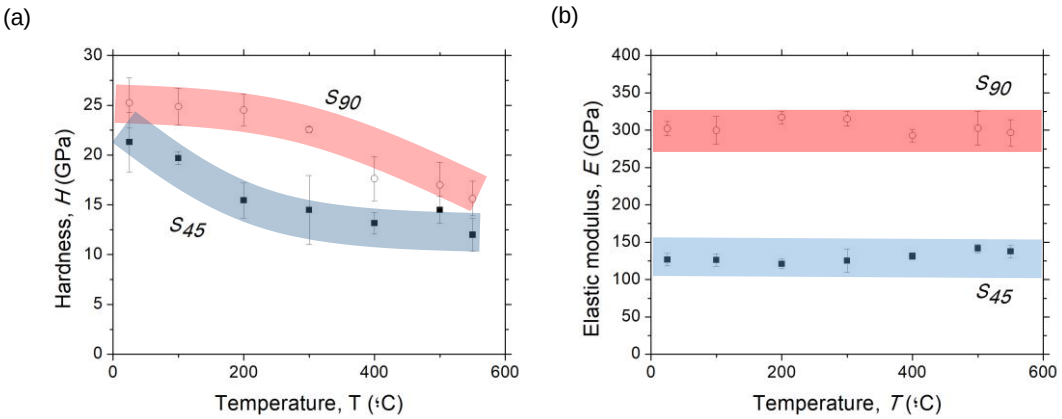

Figure 9. Micromechanical properties evolution as a function of the temperature. (a) Hardness, and (b) Elastic modulus.

3.3. Damage events

The surface damage induced at the macrometer length scale by the Vickers indenter at 1 and 10 kgf was visualized by FESEM (**Figure 10a** and **10b**, respectively). For the residual imprints performed at 1kgf, only the one corresponding to the 0º oriented sample shows clear damage affecting the whole

imprint in the form of chipping as mentioned in **section 3.2**. In contrast, at 10 kgf, a decohesion mechanism can be clearly appreciated on the S_{45} sample at the edge of the two sides of the residual imprint (labeled as (1) in **Figure 10b**), while the S_{90} sample surface around the imprint does not show signs of damage. Regarding the S_0 specimen, a similar catastrophic chipping behavior as with lower loads is observed.

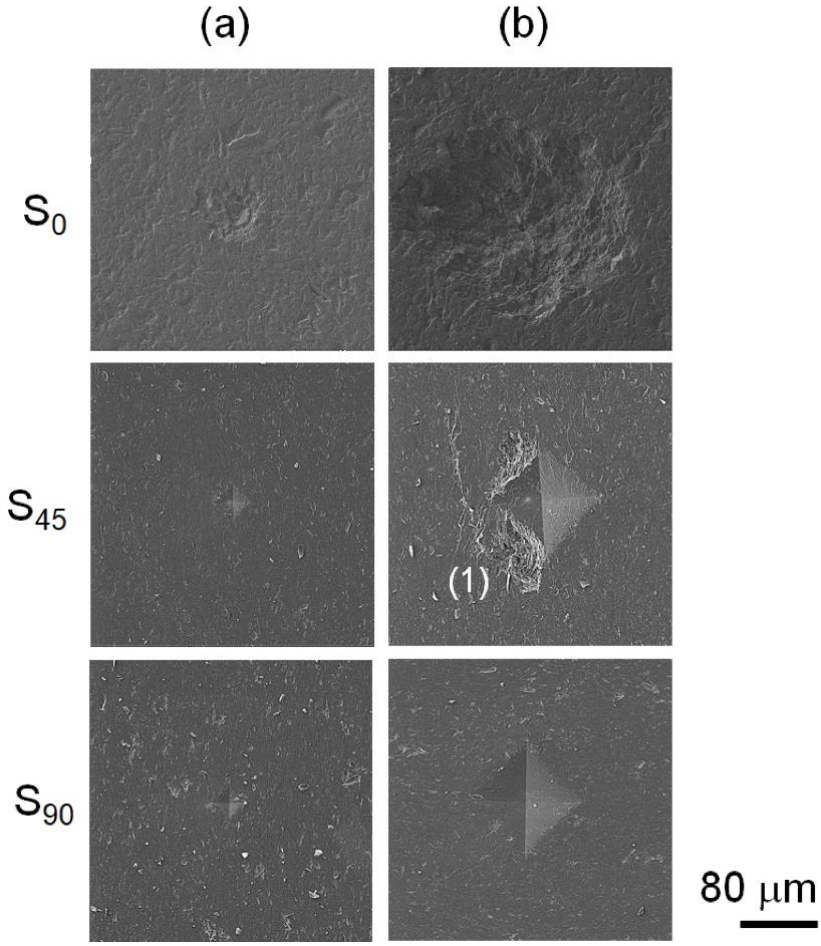

Figure 10. FESEM micrograph of the residual imprint performed under loading control mode at the macrometric length scale by using a Vickers tip indenter for each ceramic/ceramic system. (a) 1 kgf, and (b) 10 kgf.

In **Figure 11a**, the Berkovich imprint performed at 2000 nm of maximum displacement into the surface can be observed. No fracture events (i.e. radial cracks, chipping, etc.) can be observed in the vicinity of the residual imprint.

To better understand the fracture mechanisms induced at the nanometer length scale, the fractured samples were observed by FESEM though the FIB cross-section image for each architecture (**Figure 11**). The principal damage mechanism —crack deflection— takes place mainly at the platelets' interface. The FIB cross-sections were prepared at the center of the residual Berkovich impressions (white dashed line in **Figure 11a**) and a low and high fracture

damage events could be seen (FESEM micrographs of **Figure 11b** and **11c**, respectively). It is clear that the initiation and propagation of cracks occur during the loading and unloading processes, depending on the test material and also on the applied stress field [35]. Furthermore, it is possible to see that the cracks are confined inside the induced plastic field (**Figure 11b)**, which ranges between 7 to 10 times the maximum penetration depth.

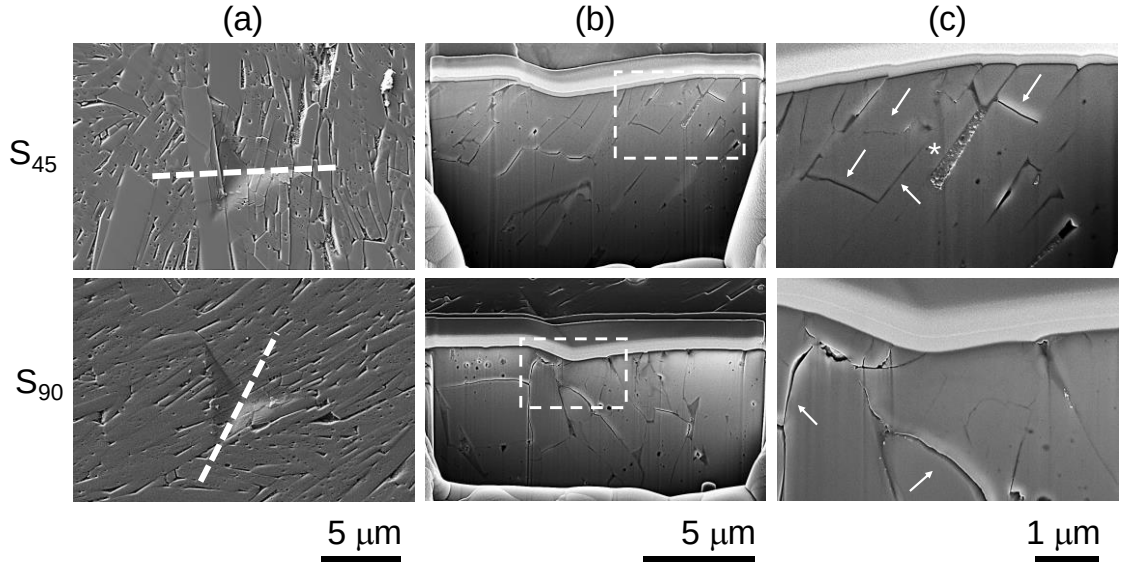

Figure 11. (a) FESEM micrographs of the ceramic/ceramic composite performed at 2000 nm of maximum displacement into surface of the S_{45} and S_{90} samples (the white dashed line shows the region were the milling process was done); (b) and (c) are the corresponding FIB cross-sectional images of the Berkovich indented surface at two different magnifications (white dash rectangle in **Figure 11b** denotes the zone observed at high magnification and presented in **Figure 11c**). Some fracture events (cracks though the interface) and glassy phase are indicated by arrows and * respectively in **Figure 11c**.

Micrographs corresponding to the region near the center of the residual imprint are shown in **Figure 11c**. The induced microcracks run parallel to both types of interfaces: Al_2O_3-platelet/glassy and Al_2O_3-platelet/Al_2O_3-platelet. Moreover, all Al_2O_3-platelet/Al_2O_3-platelet interfaces are affected by compressive loading, pointing out that they are weak links in these ceramic/ceramic composites. In addition, for the S_{45} specimen the crack propagation is stopped when the crack interacts with a glassy phase pool, see * in **Figure 11c**. The cracks deflect through both types of interfaces (Al_2O_3-platelet/glass and Al_2O_3-platelet/Al_2O_3-platelet). This phenomenon may be related to two different factors: *i)* mismatch of thermal expansion coefficients between both constitutive phases, which can produce a residual stress field and *ii)* interface adhesion strength. These factors are mainly responsible for inducing the debonding at the interface, as mentioned by Evans *et al.* [36]. The fracture along the ceramic/ceramic interface is governed

mainly by the combination of the elastic mismatch, which can be modeled following the Dundurs equation, and plastic mismatch across it. The discrepancy between both constitutive phases can be estimated by considering isotropic layers and/or platelets, as follows [37]:

$$D_{\propto} = \frac{\overline{E_1} - \overline{E_2}}{\overline{E_1} + \overline{E_2}}$$

and

$$D_{\beta} = \frac{1}{2}\frac{\mu_1(1 - 2 \cdot v_2) - \mu_2(1 - 2 \cdot v_1)}{\mu_1(1 - 2 \cdot v_2) + \mu_2(1 - 2 \cdot v_1)}$$

where $\bar{E}$ and μ are determined as:

$$\bar{E} = \frac{E}{(1 - v^2)} \qquad and \qquad \mu = \frac{E}{2 \cdot (1 + v)}$$

The indexes 1 and 2 are related to Al_2O_3-platelets and glassy phase respectively, *E* is the elastic modulus for the material of each constitutive phase. $E_{Al2O3\text{-}platelets}$ = 300 GPa [38] while $E_{glassy\ phase}$ is obtained by using the rule of mixtures as follows: $E_{glassy\ phase} = 0.52 \cdot E_{Al2O3} + 0.44 \cdot E_{SiO2} + 0.04 \cdot E_{CaO}$ = 256.48 GPa [29, 38, 39]). ν is the Poison's ratio (0.21 [38] and 0.26 obtained by using the rule of mixtures as for the elastic modulus [29] for the Al_2O_3-platelets and for the glassy phase, respectively). Then, by using the equations presented above, the D_{α} and D_{β} parameters (also known as a mismatch factors) for the systems of interest are 0.23 and 0.08, respectively. When $D_{\alpha} \neq D_{\beta}$, the nucleated crack will be expected to grow and propagate through the Al_2O_3-platelet until it reaches the interface. But, once there, it will propagate through the interface. This is in good agreement with the observation in **Figure 11**.

Finally, from these results it is possible to elucidate how the interface plays a crucial role in improving the fracture toughness of these materials and to shed some light into the relationship between the platelets orientation and the mechanical properties under different stress fields.

The assessment of fracture toughness via conventional indentation fracture toughness equations [40,41,42,43] is not possible in these materials as the Vickers residual imprints do not present well-developed radial cracks (**Figure 10** and **Figure 11a**). It should be highlighted that "*hard systems*", where cracking has been discerned by similar nanoindentation testing (i.e. using cube-corner tips), involve materials whose indentation fracture toughness ranges from 1 to 9 MPa·√m; such as titanium and chromium nitride films [44,45], alumina/mullite environmental barrier coatings [46], metal carbides [47], Zr-Si-N films [48], WC-Co [49], among others.

It is possible to estimate the fracture toughness from the *H/E* ratio, a parameter related to the elastic strain to failure and to toughness as reported in Refs. [50,51,52,53]. Several years ago, Oberle [54] recognized that this parameter is also in good agreement with the wear resistance. Furthermore, this ratio is widely quoted as a key measure to determine the limit of elastic behavior in a surface contact for the avoidance of wear [55] and can be used to estimate the fracture toughness and the wear resistance for different coatings systems. However, no information is available in the literature for the Al_2O_3-platelets/glassy phase as a function of the Al_2O_3-platelets orientation.

In **Figure 12**, the *H/E* ratio for the composite material is plotted as a function of the Al_2O_3-platelets orientation by using the nanoindentation data obtained at 2000 nm of maximum displacement into surface or maximum load of 650 mN and it is summarized in **Table 1**. The *H/E* ratio ranges between $5.4 \cdot 10^{-2}$ and $6.0 \cdot 10^{-2}$ for the S_{45} and S_{90}, respectively. From these values it can be appreciated that the S_{90} system should present a slightly greater wear resistance than S_{45}. However, this increase is not high enough to be significant. Ultimately, it can be seen that the *H/E* ratio of these ceramic/ceramic composite under consideration is in between TiN [56,57] $\left({}^{H}/_{E} = {}^{21\ GPa}/_{330\ GPa} = 9.1 \cdot 10^{-2}\right)$ with a fracture toughness of 9.9 MPa·√m and WC particles with an orientation near the basal plane $\left({}^{H}/_{E} = {}^{25.6\ GPa}/_{532\ GPa} = 4.8 \cdot 10^{-2}\right)$ with a fracture toughness of 7.2 MPa·√m [58]. Since the *H/E* reported for the Al_2O_3-platelets/glassy phase is close to that reported for the WC particles, the fracture toughness of the system under study is estimated to be in the 7.2—9.9 MPa·√m range. The obtained result is in good agreement with that reported at the macroscopic length scale by Bouville *et*

al. [23] obtained by means of Single-edged notched beam tests and obtaining a fracture toughness of around 6.2 MPa·√m. On the other hand, the reported value of fracture toughness of around 5 MPa·√m for an alumina-polymethyl methacrylate specimen processed by freeze-casted and subsequently pressed to form the “brick-and-mortar” structure [59].

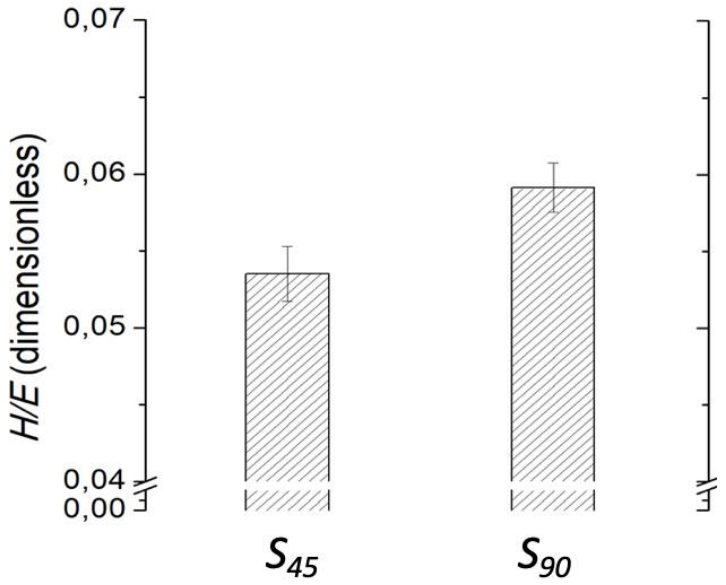

Figure 12. H/E ratio at room temperature (summarized in **Table 1**).

Figure 13 represents the *H/E* ratio for the range of tested temperatures (from RT to 550 ºC). It is worth mentioning that, due to the fact that the experiment was carried out at different conditions to that at room temperature (the applied force is larger in the latter), the *H/E* at 25 ºC differs from the one showed on **Figure 12** as a consequence of the indentation size effect. In order to further investigate the anisotropy in the deformation of the composite, the plasticity for both platelets’ orientations (S_{45} and S_{90}) was measured and compared over the whole range of temperatures, up to 550 ºC. As the temperature increases, the plasticity of S_{45} becomes gradually more pronounced than that of S_{90} up to the maximum temperature investigated here. The plasticity index and as a consequence the fracture toughness reduces when the temperatures increases may be the result of changes in the Al_2O_3 strength and/or the glassy phase softening. A similar trend was observed for a ceramic/metallic composite when the temperature increases as found in Ref. [60].

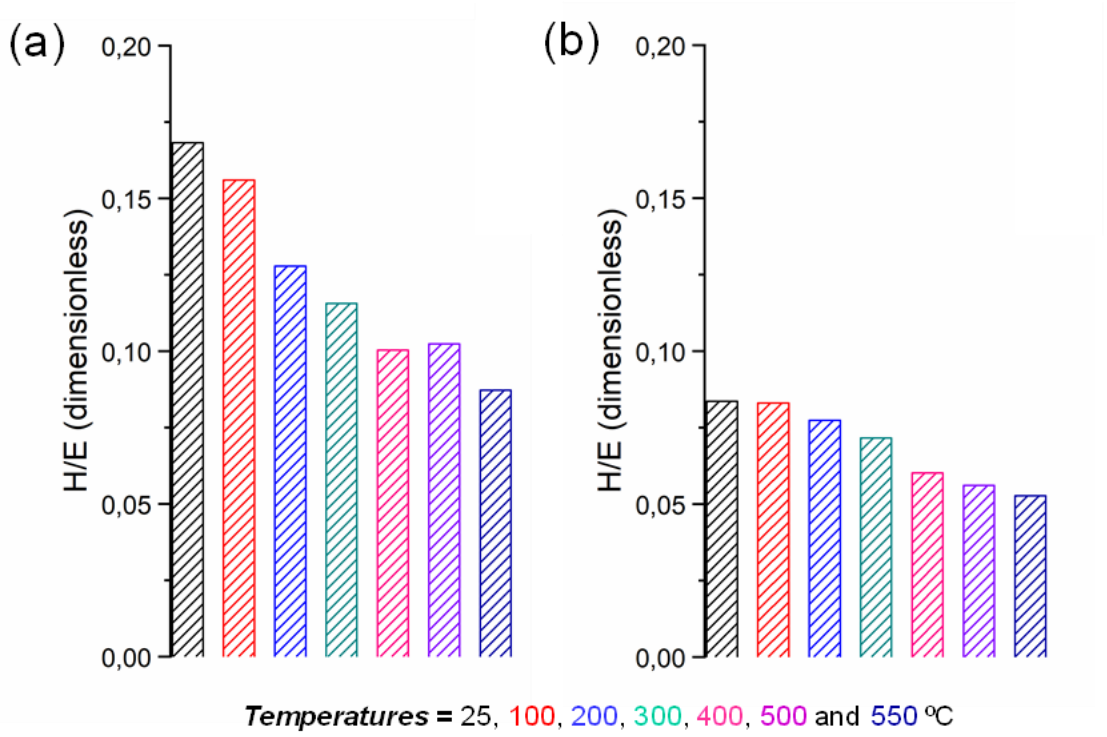

Figure 13. H/E ratio at increasing temperature for the a) S_{45} and b) S_{90}.

4. Conclusions

In this study, the microstructure and the micro- and submicrometric properties, in terms of hardness and elastic modulus, from room temperature up to 550 ºC as well as the induced damage produced during the indentation process were investigated in detail as a function of the Al_2O_3-platelet orientation. The following conclusions can be drawn:

(i) Hardness and elastic modulus values were assessed in the 21—24 GPa and 400—426 GPa ranges respectively for the Al_2O_3-platelets/glassy phase composite system determined by Berkovich nanoindentation at RT. The micromechanical properties at intermediate temperatures are strongly anisotropic. The Al_2O_3-platelets oriented at 90º are harder and stiffer than those oriented at 45º.

(ii) The influence of the platelet microstructure leads to an enhancement of the fracture toughness, with crack deflection being the main deformation mechanism. This fracture mechanism is affected by the elastic mismatch between platelets and the non-linear stress distribution present along the ceramic/ceramic composite material.

(iii) The experimental results point out a beneficial synergic effect associated with the multilayer configuration.

(iv) The *H/E* ratio assessed for the Al_2O_3-platelets/glassy phase at RT is isotropic showing a value ranging between $5.4 \cdot 10^{-2}$ and $6.0 \cdot 10^{-2}$, which is comparable to that exhibited by WC particles with a crystallographic orientation near the basal plane. The fracture toughness for the Al_2O_3-platelets/glassy phase could thus be estimated in the 7.2 – 9.9 MPa·√m range. Likewise, it would point out a comparable wear resistance for these two systems.

Acknowledgements

J. J. Roa acknowledges the Serra Hunter program of the Generalitat de Catalunya. S. Deville and H. Saad acknowledge the financial support from Agency National de la Recherche, project BICUIT (ANR-16-CE08-0006).

References

[1] S. H. Yoon, S. Park. A mechanical analysis of woodpecker drumming and its application to shock-absorbing systems. *Bioinspiration & Biomimetics.* 6 (2011) 016003.

[2] A. K. Dastjerdi, R. Rabiei, F. Barthelat. The weak interfaces within tough natural composites: experiments on three types of nacre. *J. Mechan. Beh. Bio. Mater.* 19 (2013) 50.

[3] F. Barthelat. Nacre from mollusk shells: a model for high-performance structural materials. *Bioinpiration & Biomimetics*. 5 (2010) 035001.

[4] Z. Han, J. Zhang, C. Ge, Y. Lü, J. Jiang, Q. Liu, L. Ren. Anti-erosion function in animals and its biomimetic application. *J. Bionic Eng.* 7 (2010) S50.

[5] R. E. Shadwick. Mechanical design in arteries. *J. Exp. Bio.* 202 (1999) 3305.

[6] R. M. Kulin, P. Y. Chen, F. Jiang, J. McKittrick, K. S. Vecchio. Dynamic fracture resilience of elk antler: Biomimetic inspiration for improved crashworthiness. *JOM J. Min., Met. Mat. Soc.* 62 (2010) 41.

[7] P. Y. Chen, A. G. Stokes, J. Mckittrick. Comparison of the structure and mechanical properties of bovine femur bone and antler of the North American elk (Cervus elphus Canadensis). *Acta Biomater.* 5 (2009) 693.

[8] P. Zioupos, X. T. Wang, J. D. Currey. Experimental and theoretical quantification of the development of damage in fatigue tests of bone and antler. *J. Biomechan.* 29 (1996) 989.

[9] T. Landete-Castillejos, J. D. Currey, J. A. Estevez, E. Gaspar-López, A. Garcia, L. Gallego. Influence of physiolofical effort of growth and chemical composition on antler bone mechanical properties. *Bone* 41 (2007) 794.

[10] G. N. Karam, L. J. Gibson. Biomimicking of animal quills and plant stems: natural cylindrical shells with foam cores. *Mat. Sci. Eng. C* 2 (1994) 113.

[11] M. A. Kasapi, J. M. Gosline. Micromechanics of the equine hoof wall: optimizing crack control and material stiffness through modulation of the properties of keratin. *J. Exp. Biol.* 202 (1999) 377.

[12] M. A. Kasapi, J. M. Gosline. Design complexity and fracture control in the equine hoof wall. *J. Exp. Biol.* 200 (1997) 1639.

[13] G. Bigatti, M. Giraud-Billoud, I. A. Vega, P. E. Penchaszadeh, A. Castro-Vazquez. The calcareous egg capsule of the PAtagonian neogastropod. Odontocymbiola magellanica: morphology, secretion and mineralogy. *J. Molluscan Studies.* 76 (2010) 279.

[14] S. Gayathri, R. Lakshminarayanan, J. C. Weaver, D. E. Morse, R. M. Kini, S. Valiyaveettil. In vitro study of magnesium-calcite biomineralization in the skeletal materials of the seastar Pisaster giganteus. Chemistry-A Eur. J. 13 (2007) 3262.

[15] S. N. Monteiro, R. J. S. Rodriguez, L. L. D. Costa, T. G. R. Portela, N. S. S. Santos. Thermal behavior of buriti biofoam. *Matéria* 15 (2010) 104.

[16] S. F. Fischer, M. Thielen, R. R. Loprang, R. Seidel, C. Fleck, T. Speck, A. Bührig-Polaczek. Pummelos as concept generators for biomimetically inspired low weight structures with excellent damping properties. *Adv. Eng. Mater.* 12 (2010) B658.

[17] L. Köhler, H. C. Spatz. Micromechanics of plant tissues beyond the linear-elastic range. *Planta* 215 (2002) 33.

[18] C. Morvan, C. Andème-Onzighi, R. Girault, D. S. Himmelsbach, A. Driouich, D. E. Akin. Building flax fibers: more than one brick in the walls. *Plant Physiology and Biochemistry* 41 (2003) 935.

[19] M. A. R. Koehl, S. A. Wainwright. Mechanical adaptations of a giant kelp. *Limnology and Oceanography* 22 (1977) 1067.

[20] P. I. B. G. B Pelissari, V. C. Pandolfelli, D. Carnelli, F. Bouville. Refractory interphase and its role on the mechanical properties of boron containing nacre-like ceramic. *J. Eur. Ceram. Soc.* 40 (2019) 165.

[21] P. I. B. G. B. Pelissari, F. Bouville, V. C. Pandolfelli, D. Carnelli, F. Giuliani, A. P. Luz, E. Saiz, A. R. Studart. Nacre-like ceramic refractories for high temperature applications. *J. Eur. Ceram. Soc.* 38 (2018) 2186.

[22] H. Le Ferrand, F. Bouville, T. P. Niebel, A. R. Studart. Magnetically assisted slip casting of bioinspired heterogeneous composites. *Nat. Mater.* 14 (2015) 1.

[23] F. Bouville, E. Maire, S: Meille, B. Van de Moortèle, A. J. Stevenson, S. Deville. Strong, tough and stiff bioinspired ceramics from brittle constituents. *Nat. Mater.* 13 (2014) 508.

[24] M. Mirkhalaf, A. Khayer Dastjerdi, F. Barthelat. Overcoming the brittleness of glass through bio-inspiration and micro-architecture. *Nat. Comm.* 5 (2014) 3166/1.

[25] L. J. Bonderer, A. R. Studart, L. J. Gauckler. Bioinspired design and assembly of platelet reinforced polymer films. *Science* 319 (2008) 1069.

[26] S. Deville, F. Bouville, A. Stevenson. Ceramic product with oriented particles and method for the production thereof. US20170129816A1 (2014).

[27] K. Radi, H. Saad, D. Jauffres, S. Meille, T. Douillard, S. Deville, C. L. Martin. Effect of microstructure heterogeneity on the damage resistance of nacre-like alumina: Insights from image-based discrete simulations. *Scr. Mater.* 191 (2021) 210.

[28] A. Doitrand, R. Henry, H. Saad, S. Deville, S. Meille. Determination of interface fracture properties by micro- and macro-scale experiments in nacre-like alumina. *J. Mechan. Phys. Sol.* 145 (2020) 104143.

[29] W. C. Oliver, G. M. Pharr. Improved technique for determining hardness and elastic modulus using load and displacement sensing indentation experiments. *J. Mater. Res.* 7 (1992) 1564.

[30] W. C. Oliver, G. M. Pharr. Measurement of hardness and elastic modulus by instrumented indentation: advances in understanding and refinements to methodology. *J. Mater. Res.* 19 (2004) 3.

[31] W. D. Nix, H. Gao. Indentation size effects in crystalline materials: a law for strain gradient plasticity. *J. Mechan. Phys. Sol.* 46 (1998) 411.

[32] H. Le Ferrand, F. Bouville. Processing of dense bioinspired ceramics with deliberate microstructure. *J. Am. Ceram. Soc.* 102 (2019) 7253.

[33] R. Pratyush Behera, S. Bin Senin Muhammad, M. He Jiaxuan, H. Le Ferrand. Porous textured ceramics with controlled grain size and orientation. *J. Eur. Ceram. Soc.* 41 (2021) 617.

[34] M. Ciccotti, F. Mulargia. Differences between static and dynamic elastic moduli of a typical seismogenic rock. *Geophys. J. Int.* 157 (2004) 474.

[35] R. F. Cook, G. M. Pharr. Direct observation and analysis of indentation cracking in glasses and ceramics. *J. Am. Ceram. Soc.* 73 (1990) 603.

[36] A. G. Evans, J. W. Hutchinson. The thermomechanical integrity of thin films and multilayers. Acta Metall. Mater. 43 (1995) 2507.

[37] J. W. Hutchinson, Z. Suo. Mixed mode cracking in layered materials. *Adv. Appl. Mech.* 29 (1992) 63.

[38] D. de Faoite, D. J. Browne, F. R. Chang-Díaz, K. T. Stanton. A review of the processing, composition, and temperature-dependent mechanical and thermal properties of dielectric technical ceramics. *J. Mater. Sci.* 47 (2012) 4211.

[39] Q. Liu, Q. He. Elastic constants for various classes of solids at high temperature. *Acta Phys. Polonica A.* 112 (2007) 69.

[40] B. R. Lawn, A. Evans, D. Marshall. Elastic/plastic indentation damage in ceramics: the median/radial crack system. *J. Am. Ceram. Soc.* 63 (1980) 574.

[41] G. Pharr. Measurement of mechanical properties by ultra-low load indentation. *Mater. Sci. Eng. A*. 253 (1998) 151.

[42] K. Niihara. A fracture mechanics analysis of indentation-induced Palmqvist crack in ceramics. *J. Mater. Sci. Lett.* 2 (1983) 221.

[43] G. R. Anstis, P. Chantikul, B. R. Laen, D. B. Marshall. A critical evaluation of indentation techniques for measuring fracture toughness: I. Direct crack measurements. *J. Am. Ceram. Soc.* 64 (1981) 533.

[44] K. Holmberg, H. Ronkainen, A. Laukkanen, K. Wallin, S. Hogmark, S. Jacobson, U. Wiklund, R. M. Souza, P. Stahle. Residual stresses in TiN, DLC and MoS2 coated surfaces with regard to their tribological fracture behabiour. *Wear* 267 (2009) 2142.

[45] M. Sebastiani, K. E. Johanns, E. G. Herbert, G. M. Pharr. Measurement of fracture toughness by nanoindentation methods: Recent advances and future challenges. *Current Opinion in Solid Stat. Mater. Sci.* 19 (2015) 324.

[46] C. A. Botero, E. Jiménez-Piqué, J. Seuba, T. Kulkarni, V. K. Sarin, L. Llanes. Mechanical behaviour of $3Al_2O_3{\cdot}2SiO_2$ films under nanoindentation. *Acta Mater.* 60 (2012) 5889.

[47] D. Casellas, J. Caro, S. Molas, J. M. Prado, I. Valls. Fracture toughness of carbides in tool steels evaluated by nanoindentation. *Acta Mater.* 55 (2007) 4277.

[48] K. Yalamanchili, R. Forsén, E. Jiménez-Piqué, M. P. Johansson Jöesaar, J. J. Roa, N. Ghafoor, M. Odén. Surface, deformation and fracture of arc evaporated Zr-Si-N hard films. *Surf. Coat. Technol.* 256 (2014) 1100.

[49] J. J. Roa, P. Sudharshan Phani, W. C. Oliver, L. Llanes. Mapping of mechanical properties at microstructural length scale in WC-Co cemented carbides: Assessment of hardness and elastic modulus by means of high speed massive nanoindentation and statistical analysis. *Int. J. Refract. Met. Hard Mater.* 75 (2018) 211.

[50] A. Leyland, A. Matthews. Design criteria for wear-resistant nanostructured and glassy-metal coatings. *Surf. Coat. Technol.* 177-178 (2004) 317.

[51] A. Leyland, A. Matthews. On the significance of the H/E ratio in wear controls: a nanocomposite coating approach to optimized tribological behavior. *Wear* 246 (2000) 1.

[52] H. W. Strauss, R. R. Chromik, S. Hassani, J. E. Klemberg-Sapieha. In situ tribology of nanocomposite Ti-Si-C-H coatings prepared by PE-CVD. *Wear* 272 (2011) 133.

[53] E- Frutos, A. Cuevas, J. L. González-Carrasco, F. Martín. Characterization of the elastic-plastic behavior of intermetallic coatings growth on medical stainless Steel by instrumented ultramicroindentation. *J. Mechan. Beh. Biomed. Mater.* 16 (2012) 1.

[54] T. L. Oberle. Wear of metals. *J. Met.* 3 (1951) 438.

[55] J. Halling. Surface films in tribology. *Tribologia.* 1 (1982) 15.

[56] D. Diao, K. Kato, K. Hokkirigawa. Fracture mechanisms of ceramic coatings in indentation. *J. Tribol.* 116 (1994) 860.

[57] E. Török, A. Perry, L. Chollet, W. Sproul. Young's modulus of TiN, TiC, ZrN and HfN. *Thin Sol. Films*. 153 (1987) 37.

[58] N. Cuadrado, D. Casellas, L. Llanes, I. Gonzalez, J. Caro. Effect of cristal anisotropy on the mechanical properties of WC embedded in WC-Co cemented

carbides, in *Proceedings of the Euro PM2011 Powder Metallurgy Congress & Exhibition. 2011, pp. 215.*

[59] E. Munch, M. E. Launey, D. H. Alsem, E. Saiz, A. P. Tomsia, R. O. Ritchie. Though, Bio-Inspired Hybrid Materials. *Science* 322 (2008) 1516.

[60] A. Vornberger, J. Pötschke, T. Gestrich, M. Herrmann, A. Michaelis. Influence of microstructure on hardness and thermal conductivity of hardmetals. *International Journal of Refractory Metals and Hard Materials*. 88 (2020) 105170/1.